Translational Oncology
www.transonc.com

Volume 3 Number 5 October 2010 pp. 307–317 307

Detection of Cancer Metastases with a Dual-labeled Near-Infrared/Positron Emission Tomography Imaging Agent[1,2]

Lakshmi Sampath*,†, Sunkuk Kwon*, Mary A. Hall*, Roger E. Price‡ and Eva M. Sevick-Muraca*

*Center for Molecular Imaging, Institute of Molecular Medicine, University of Texas Health Science Center, Houston, TX, USA; †Molecular Physiology and Biophysics, Baylor College of Medicine, Houston, TX, USA; ‡Center for Comparative Medicine, Baylor College of Medicine, Houston, TX, USA

Abstract

By dual labeling a targeting moiety with both nuclear and optical probes, the ability for noninvasive imaging and intraoperative guidance may be possible. Herein, the ability to detect metastasis in an immunocompetent animal model of human epidermal growth factor receptor 2 (HER-2)–positive cancer metastases using positron emission tomography (PET) and near-infrared (NIR) fluorescence imaging is demonstrated. *METHODS:* $(^{64}\text{Cu-DOTA})_n$-trastuzumab-$(\text{IRDye800})_m$ was synthesized, characterized, and administered to female Balb/c mice subcutaneously inoculated with highly metastatic 4T1.2neu/R breast cancer cells. $(^{64}\text{Cu-DOTA})_n$-trastuzumab-$(\text{IRDye800})_m$ (150 μg, 150 μCi, $m = 2$, $n = 2$) was administered through the tail vein at weeks 2 and 6 after implantation, and PET/computed tomography and NIR fluorescence imaging were performed 24 hours later. Results were compared with the detection capabilities of F-18 fluorodeoxyglucose (^{18}FDG-PET). *RESULTS:* Primary tumors were visualized with ^{18}FDG and $(^{64}\text{Cu-DOTA})_n$-trastuzumab-$(\text{IRDye800})_m$, but resulting metastases were identified only with the dual-labeled imaging agent. ^{64}Cu-PET imaging detected lung metastases, whereas *ex vivo* NIR fluorescence showed uptake in regions of lung, skin, skeletal muscle, and lymph nodes, which corresponded with the presence of cancer cells as confirmed by histologic hematoxylin and eosin stains. In addition to detecting the agent in lymph nodes, the high signal-to-noise ratio from NIR fluorescence imaging enabled visualization of channels between the primary tumor and the axillary lymph nodes, suggesting a lymphatic route for trafficking cancer cells. Because antibody clearance occurs through the liver, we could not distinguish between nonspecific uptake and liver metastases. *CONCLUSION:* $(^{64}\text{Cu-DOTA})_n$-trastuzumab-$(\text{IRDye800})_m$ may be an effective diagnostic imaging agent for staging HER-2–positive breast cancer patients and intraoperative resection.

Translational Oncology (2010) 3, 307–317

Introduction

Molecular imaging with target-specific moieties conjugated to optical and nuclear reporters enables visualization of disease markers using noninvasive techniques, whereas optical reporters can additionally provide information for image-guided surgical procedures. Previously, we and others have synthesized and characterized dual-labeled peptide and antibody-based imaging agents in subcutaneous xenograft animal models [1–13]. In two of these studies [3,14], optical and nuclear imaging showed comparable tumor-to-muscle ratios (TMRs) after intravenous administration of a dual-labeled agent, whereas near-infrared (NIR) fluorescence optical imaging provided a significantly higher signal-to-noise ratio than gamma imaging. In this study, we designed a positron emission tomography (PET)/NIR imaging agent—$(^{64}\text{Cu-DOTA})_n$-trastuzumab-$(\text{IRDye800})_m$—which consists of an antibody (trastuzumab) dual labeled with a beta emitter (Cu-64) for PET imaging and a NIR dye (IRDye 800CW) to enable fluorescence imaging of metastatic lesions overexpressing the human epidermal growth factor receptor 2 (HER-2). We used a syngeneic mouse model of an orthotopic mammary fat pad implantation, which exhibits

Address all correspondence to: Eva M. Sevick-Muraca, PhD, University of Texas Health Science Center, 1825 Pressler St, SRB 330A, Houston, TX 77030.
E-mail: Eva.Sevick@uth.tmc.edu

[1]This work is supported in parts by R01 CA112679-15 (E.M.S.-M.), U54 136404-01 (E.M.S.-M.), the Texas STAR Award program, and Department of Defense predoctoral fellowship award BC073377 (L.S.). Cu-64 provided by Washington University, St. Louis, MO, was partially funded by National Cancer Institute grant R24 CA86307.
[2]This article refers to supplementary material, which is designated by Table W1 and is available online at www.transonc.com.
Received 10 May 2010; Revised 7 June 2010; Accepted 14 June 2010

DOI 10.1593/tlo.10139

metastases to organs similar to those affected in late-stage breast cancer. We used this model to test the ability of the dual-labeled imaging agent to detect metastases in sites distant from the primary tumor.

HER-2 is overexpressed because of gene amplification in approximately 20% to 30% of breast cancer patients, often leading to poor prognosis [15]. HER-2 is predominantly conserved during metastases [16–19], making it a potential diagnostic biomarker. Trastuzumab (Herceptin; Genentech, Inc, San Francisco, CA) is a humanized anti–HER-2 antibody approved as a clinical therapeutic [20]. Trastuzumab has been labeled by numerous investigators to generate imaging agents with applications including but not limited to nuclear, optical, and multimodal imaging (see Table W1). Yet to date, preclinical *in vivo* characterization of its use as an imaging agent has predominantly focused on subcutaneous tumor models using athymic mice.

Although the xenograft animal model is well established in cancer research to provide information regarding the interaction between the exogenously administered agent and the cancer cells *in vivo*, subcutaneous implantation of cancer cells neither realistically reproduces the microenvironment around the tumor region nor enables determination of whether the imaging agent can detect metastases in deep tissue organs. Xenograft models can approximate primary tumor growth in mice, but murine tumor models with normal immune function may be better suited to demonstrate detection of metastases. In this study, we use a syngeneic mouse model in which HER-2 expressing mammary cancer cells are introduced orthotopically into the mammary fat pad to mimic late-stage human breast cancer metastases. We have used this animal model to test the ability of the dual-labeled imaging agent to detect metastases in sites distant from the primary tumor and to compare to the clinical criterion standard of ^{18}FDG-PET.

Materials and Methods

We purchased trastuzumab for research purposes at the hospital pharmacy and used it before the date of expiration. Trastuzumab was stored at 4°C. IRDye 800CW was purchased from LI-COR Biosciences (Lincoln, NB) and p-SCN-Bn-DOTA was purchased from Macrocyclics (Dallas, TX).

Synthesis of (DOTA)$_n$-Trastuzumab-(IRDye800)$_m$

Trastuzumab was conjugated with p-SCN-Bn-DOTA using a previously reported protocol with slight modifications [21]. In brief, trastuzumab was dissolved in HEPES buffer (0.1 M, pH 8.5) at a concentration of 10 mg/ml and mixed with 20-molar excess of p-SCN-Bn-DOTA (25 mg/ml) dissolved in ethanol. The reaction mixture was incubated at 4°C overnight. Purification of (DOTA)$_n$-trastuzumab from excess chelator was achieved by using Zeba desalting columns (Pierce Biotechnology, Rockford, IL) with PBS in the mobile phase. Final concentration was measured based on UV absorbance at 280 nm using spectrophotometric analysis (model DU-800 instrument; Beckman Coulter, Brea, CA). (DOTA)$_n$-trastuzumab (5 mg/ml) was then reacted with IRDye 800CW (30 μg/mg protein) dissolved in dimethyl sulfoxide (50 μl/mg dye) at 4°C for 2 to 3 hours. (DOTA)$_n$-trastuzumab-(IRDye800)$_m$ was purified from free dye using Zeba desalting columns.

Radiolabeling of (DOTA)$_n$-Trastuzumab-(IRDye800)$_m$

^{64}Cu was obtained from Washington University Medical School (St Louis, MO) and supplied at high specific activity as $^{64}CuCl_2$ in 0.1 M HCl. For radiolabeling, $^{64}CuCl_2$ was diluted in ammonium acetate buffer (0.2 M, pH 5.5) at 50 mCi/ml and added to (DOTA)$_n$-trastuzumab-(IRDye800)$_m$. The reaction mixture was incubated at 50°C for 1 hour. (^{64}Cu-DOTA)$_n$-trastuzumab-(IRDye800)$_m$ was purified with PBS as the mobile phase using Zeba desalting columns, and radiolabeling yield was calculated using ITLC.

Determination of the Number of DOTA and IRDye800 Molecules per Trastuzumab Antibody

The average number of DOTA molecules per trastuzumab was estimated using a protocol previously described [22]. In brief, $^{64}CuCl_2$ was mixed with a defined amount of nonradioactive $CuCl_2$ carrier (80-fold excess of (DOTA)$_n$-trastuzumab-(IRDye800)$_m$) and added to 50 μg of (DOTA)$_n$-trastuzumab-(IRDye800)$_m$ in a total volume of 100 μl of 0.2 M sodium acetate buffer. The reaction mixture was incubated at 50°C for 1 hour. (^{64}Cu-DOTA)$_n$-trastuzumab-(IRDye800)$_m$ was purified using the Zeba desalting column, and radiolabeling yield was calculated. The number of DOTA molecules per trastuzumab (n) was calculated as follows:

$$(n) = \text{moles}\left(Cu^{2+}\right) \times \text{yield} / \text{moles of } (\text{DOTA})_n - \text{trastuzumab} - (\text{IRDye800})_m$$

The IRDye800 to trastuzumab ratio (m) is estimated using the absorbance measurements of the dye and protein at 778 and 280 nm, respectively, as described by the labeling protocol from LI-COR Biosciences. A correction factor of 3% was subtracted from the measurement at 280 nm because of dye contribution.

Cell Lines

Cell lines used in this study include human SKBr3 and MDA-MB-231 and murine 4T1.2, 4T1.2neu, 4T1.2R, and 4T1.2neu/R breast cancer cells. SKBr3 cells express high levels of HER-2, whereas MDA-MB-231 cells express negligible amounts of HER-2. SKBr3 and MDA-MB-231 cell lines were obtained from American Type Culture Collection (Manassas, VA). 4T1.2 is a subline of breast cancer cells derived from spontaneous carcinoma in a Balb/cfC3H mouse [23]. Because HER-2 is highly conserved across species, we used 4T1.2neu cells, which were established by transducing the rat homolog of HER-2, neu, into 4T1.2 breast cancer cells with a retroviral vector, pFB-Neu-Neo [24]. Both 4T1.2 and 4T1.2neu were generously provided by Zhaoyang You (University of Pittsburg School of Medicine, Pittsburgh, PA). We transfected both these cell lines with p-DsRedExpress-N1 (Clontech, Mountain View, CA) to generate 4T1.2R and 4T1.2neu/R which were selected by flow cytometry using a Becton-Dickinson FACS Aria flow cytometer (BD Biosciences, San Jose, CA). The DsRed-expressing cells were cultured in Dulbecco's minimal essential medium F-12 with 10% fetal bovine serum, 1% antibiotic-antimycotic solution, and 1 mg/ml of G418 in a humidified incubator maintained at 37°C with 5% CO_2.

In Vitro Microscopy

Cells were grown on coverslips in a 24-well dish. When cells reached 90% confluence, cells were washed and blocked with Odyssey Blocking Buffer (LI-COR Biosciences) for 1 hour. Cells were then incubated with primary mouse anti–HER-2 antibodies or (Cu-DOTA)$_n$-trastuzumab-(IRDye800)$_m$ diluted in Odyssey Blocking Buffer for 1 hour at 4°C. Cells were washed and stained with secondary antibodies, goat anti-mouse AlexaFluor 488 or mouse antihuman fluorescein isothiocyanate, respectively, for 30 minutes at 4°C. After this incubation period, cells were washed again, and the cover slips were placed on a glass slide with mounting medium containing 4′-6-Diamidino-2-phenylindole nuclear stain (Vectashield; Vector Laboratories, Burlingame, CA).

All images were acquired using a Leica DFC350FX microscope (Leica Microsystems, Inc, Bannockburn, IL) connected to a computer.

Images were processed using Leica Application Suite software or Image J (National Institutes of Health, Bethesda, MD).

In-cell Western Blot

4T1.2 and 4T1.2neu cells were seeded in a 96-well plate and grown overnight. Cells were fixed and blocked using Odyssey Blocking Buffer (LI-COR Biosciences) for 1 hour at room temperature. Mouse antirat HER-2/*neu* primary antibody (Calbiochem, La Jolla, CA) was diluted in blocking buffer at a concentration of 5 μg/ml and added to the cells to incubate for 2.5 hours at room temperature. Cells were washed with Tris-buffered saline and Tween 20 and IRDye 800CW–labeled goat antimouse IgG secondary antibody (LI-COR Biosciences) was added to cells at a dilution of 1:1000. For normalization of cell number, DRAQ5 (LI-COR Biosciences) diluted at 1:5000 was also added to the cells and allowed to incubate for 1 hour. After repeated washing, the wells were allowed to dry and fluorescence imaging was performed on the Odyssey infrared imaging system (LI-COR Biosciences) using the 800-nm channel to measure HER-2 expression and the 700-nm channel to normalize for cell count using fluorescence from DRAQ5.

Animal Model

Female Balb/c mice (8 weeks old; Charles River, Wilmington, MA) were housed and maintained in a specific pathogen-free colony at the Institute of Molecular Medicine, UT-Health Science Center, and were fed standard chow diet. The facility is accredited by the American Association for Laboratory Animal Care, and all experiments were performed in accordance with the guidelines of UT-Health Science Center Institutional Animal Care and Use Committee. Animals were subcutaneously injected with 4T1.2neu/R ($1\text{-}2 \times 10^6$ in 20 μl) into the fourth mammary fat pad. Initial tumor growth was monitored with DsRed fluorescence imaging. Before imaging, mice were shaved, and residual fur was removed using a depilatory agent. ^{18}FDG (200-250 μCi) or $(^{64}\text{Cu-DOTA})_n$-trastuzumab-$(\text{IRDye800})_m$ (150 μg, 150 μCi, $n = 2$, $m = 2$) were injected intravenously at week 2 in 4T1.2neu/R ($N = 5$) or at week 6 in 4T1.2R ($N = 6$), 4T1.2neu/R ($N = 6$) and non–tumor-bearing ($N = 3$) mice, for subsequent microPET/computed tomography (CT) and NIR fluorescence imaging. ^{18}FDG was injected first, and PET/CT imaging was performed. $(^{64}\text{Cu-DOTA})_n$-trastuzumab-$(\text{IRDye800})_m$- was injected after 10 half-lives of F-18 radioactive decay, followed by NIR fluorescence imaging and PET/CT approximately 24 hours later. The imaging time point was determined based on the radioactive half-life of ^{64}Cu ($t_{1/2}$ = 12.7 hours), although no significant increase in tumor uptake has been shown with NIR fluorescence imaging at time points greater than 24 hours [10]. After *in vivo* imaging techniques, mice were euthanized, and select organs were harvested for *ex vivo* NIR fluorescence imaging. For further histopathologic analysis, tissue samples were placed in 10% formalin overnight and sent to the Center for Comparative Medicine Pathology Core (Baylor College of Medicine, TX) before undergoing routine histologic processing, sectioning, and hematoxylin and eosin (H&E) staining.

In Vivo Fluorescence Imaging

NIR and DsRed fluorescence images were acquired using custom-built fluorescence imaging systems [10]. Briefly, a field of view was illuminated with 785 or 568 nm of light from a laser diode (500 mW; Intense Ltd, North Brunswick, NJ) or air-cooled argon-krypton laser (Model 643R-AP-A01, 200 mW; Melles Griot, Carlsbad, CA), respectively, outfitted with a convex lens and diffuser to create a uniform excitation field. The fluorescence was collected through holographic (model HNPF-785.0-2.0 for NIR and model 568.2-6 for DsRed; Kaiser Optical Systems, Inc, Ann Arbor, MI) and interference (model 830.0-2.0 for NIR, Image Quality [Andover Corp, Salem, NH] and model HQ610/60M for DsRed [Chroma Technology Corp, Bellows Falls, VT]) filters placed before a Nikon camera lens (Nikkor 28 mm; Nikon, Tokyo, Japan). The images were finally captured by an electron-multiplying charge-coupled device camera (PhotonMax 512; Princeton Instruments, Princeton, NJ) with 200 to 400 milliseconds of integration time. For acquisition of white-light images, the optical filters were removed, and a low-power lamp illuminated the subject. Image acquisition was accomplished by V++ software (Aukland, New Zealand).

Whole-body fluorescence images were acquired 24 hours after intravenous administration of $(^{64}\text{Cu-DOTA})_n$-trastuzumab-$(\text{IRDye800})_m$ (150 μg, 150 μCi). On sacrifice, *ex vivo* fluorescence imaging of harvested organs was also performed.

MicroPET/CT Imaging

In vivo small animal PET/CT imaging studies were performed using an INVEON dedicated PET docked with an INVEON multimodality CT (Siemens Medical Solutions, Knoxville, TN). The CT imaging parameters were an x-ray voltage of 80 kV with an anode current of 500 μA and an exposure time of 260 milliseconds of each of the 120 rotation steps over the total rotation of 220° at low system magnification. After CT imaging, PET emission scans were performed on separate days with acquisition times of 5 (^{18}F) and 10 minutes (^{64}Cu). PET and CT images were reconstructed using two-dimensional filtered back-projection and a Feldkamp cone-beam algorithm with a ramp filter cutoff at the Nyquist frequency, respectively. PET and CT image fusion and image analysis were performed using ASIPro, Inveon Research Workplace (Siemens Preclinical Solutions) and AMIRA (version 3.1; Konrad-Zuse-Zentrum fur Informationstechnik, Berlin, Germany).

Statistical Analysis

All data were analyzed using one-way analysis of variance, the significance level was set at 0.05, and all quantitative data are represented as mean ± SD. To determine TMR or lung-to-muscle ratio (LMR) from NIR fluorescence images, a region-of-interest was drawn around the tumor, lung, or muscle region, and the total fluorescence signal intensity associated with the region was computed. TMR or LMR from NIR fluorescence images was calculated as follows:

TMR or LMR = (sum of fluorescence counts in tumor or lung region / number of pixels) / (sum of fluorescence counts in muscle region / number of pixels)

To calculate TMR from PET images, tumor standardized uptake value (SUV) and the contralateral muscle SUV were computed using the Inveon Research Workplace (Siemens Preclinical Solutions). TMR calculations were performed as follows:

TMR = Tumor SUV / Muscle SUV

Results

Characterization of $(^{64}\text{Cu-DOTA})_n$-Trastuzumab-$(\text{IRDye800})_m$

Trastuzumab was conjugated to p-SCN-Bn-DOTA and IRDye 800CW, resulting in approximately 2.4 ± 0.2 DOTA molecules per

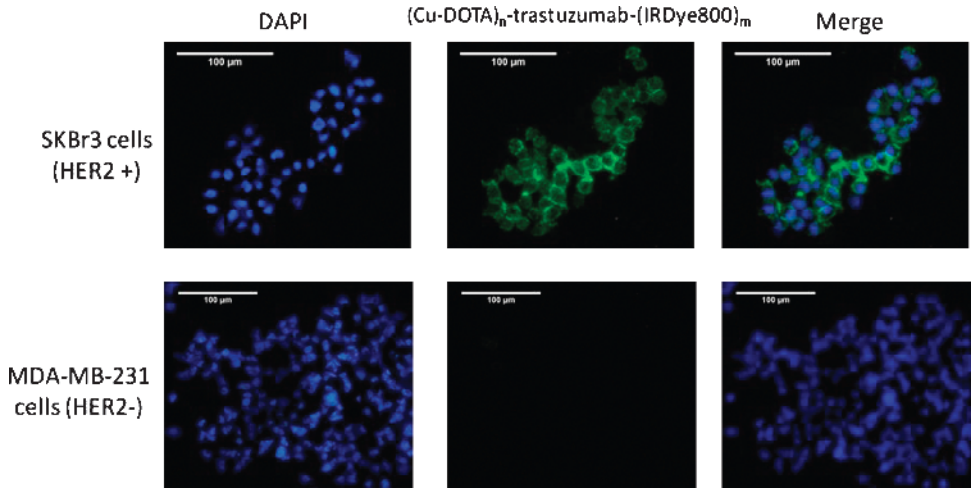

Figure 1. Fluorescence microscopy imaging shows significant binding of (Cu-DOTA)$_n$-trastuzumab-(IRDye800)$_m$ to HER-2–overexpressing SKBr3 cells in comparison to low HER-2 expressing MDA-MB-231 cells.

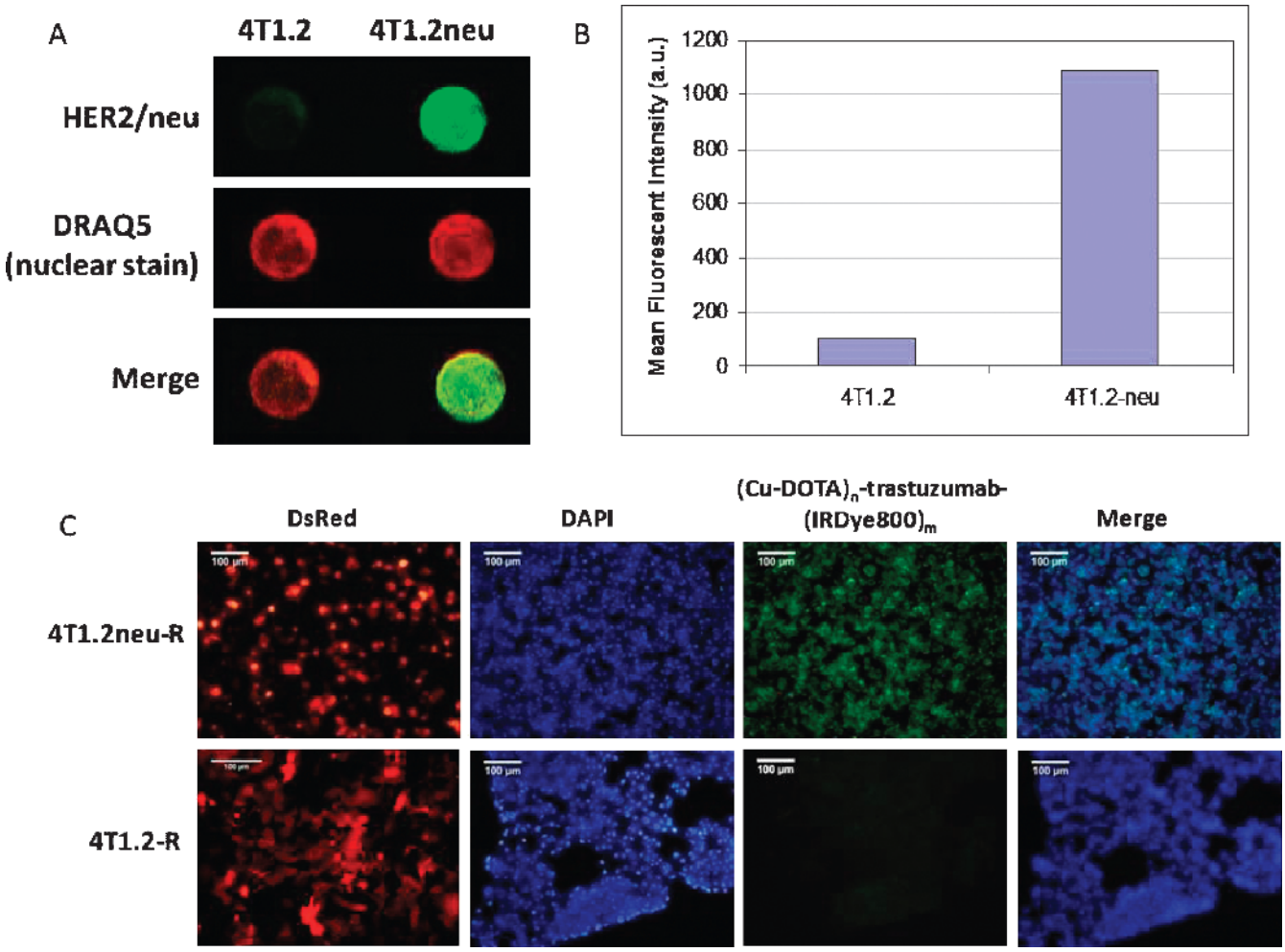

Figure 2. 4T1.2neu cells have an elevated level of HER-2/*neu* receptor density compared with 4T1.2 breast cancer cells. (A) In-cell Western blot shows fluorescence signal intensity after HER-2/*neu* staining (top panel). Cells were normalized using DRAQ5 nuclear staining (middle panel), whereas the composite merged signals are shown in the bottom panel. (B) Quantification of mean fluorescence signal intensity. (C) Fluorescence microscopy imaging shows significantly higher binding of (Cu-DOTA)$_n$-trastuzumab-(IRDye800)$_m$ in 4T1.2neu/R cells compared with 4T1.2/R.

antibody (*n*). The IRDye800 to trastuzumab ratio was 2.2 ± 0.3 (*m*). The yield of $(DOTA)_n$-trastuzumab-$(IRDye800)_m$ after purification was greater than 85%. Radiolabeling yield with Cu-64 was greater than 90%. Immunoreactivity as determined by the cell-binding assay described by Lindmo et al. [25] was determined to be 76.4% ± 3.6%.

In Vitro Characterization

Figure 1 illustrates binding of $(Cu\text{-}DOTA)_n$-trastuzumab-$(IRDye800)_m$ in SKBr3 (HER-2–overexpressing) and MDA-MB-231 (low expressors of HER-2) cells as visualized through fluorescence microscopy. The imaging agent binds with high affinity to SKBr3 cells, whereas there is negligible binding in MDA-MB-231 cells. Also, the binding seems to be extracellular, which is consistent with the location of the transmembrane HER-2 receptors. The dual-labeled imaging agent bound to greater than 90% of SKBr3 cells, as determined by NIR FACS.

Figure 2*A* represents an in-cell Western blot to quantify the difference in HER-2 levels between 4T1.2 and 4T1.2neu cells. The *top panel* in Figure 2*A* shows the fluorescence signal from HER-2/*neu* staining in cells, the *middle panel* shows the DRAQ5 nuclear staining for normalization with cell number, whereas the *bottom panel* shows the combined fluorescence signal. The quantitative results are depicted graphically in Figure 2*B*. Figure 2*C* compares the binding of $(Cu\text{-}DOTA)_n$-trastuzumab-$(IRDye800)_m$ in DsRed-transfected 4T1.2R and 4T1.2neu/R cells. Both cell lines express DsRed as illustrated, but 4T1.2neu/R has a significantly higher fluorescence because of binding of the dual-labeled imaging agent compared with 4T1.2R.

In Vivo Characterization

Because DsRed expression was lost with tumor progression, DsRed fluorescence imaging was conducted to assess inoculation and initial growth. DsRed fluorescence imaging of a shaved Balb/c mouse with a subcutaneous 4T1.2neu/R tumor confirms the location of the tumor (Figure 3*A*). The corresponding NIR fluorescence image acquired 24 hours after $(^{64}Cu\text{-}DOTA)_n$-trastuzumab-$(IRDye800)_m$ administration is shown in Figure 3*B*. PET signal fused with CT after $(^{64}Cu\text{-}DOTA)_n$-trastuzumab-$(IRDye800)_m$ and ^{18}FDG administration revealed significant uptake within the tumor compared with the muscle region. Representative coronal sections are represented in Figure 3, *C* and *D*, with crosshairs indicating tumor location. In addition to tumor uptake, the dual-labeled imaging agent accumulates within the liver, as seen in both PET and NIR fluorescence images. The nonspecific liver uptake may be attributed to the interaction of the Fc portion of the antibody with hepatocytes and is consistent with the site of antibody degradation and clearance.

Tumor uptake after ^{18}FDG and $(^{64}Cu\text{-}DOTA)_n$-trastuzumab-$(IRDye800)_m$ administration shows comparable results as observed by

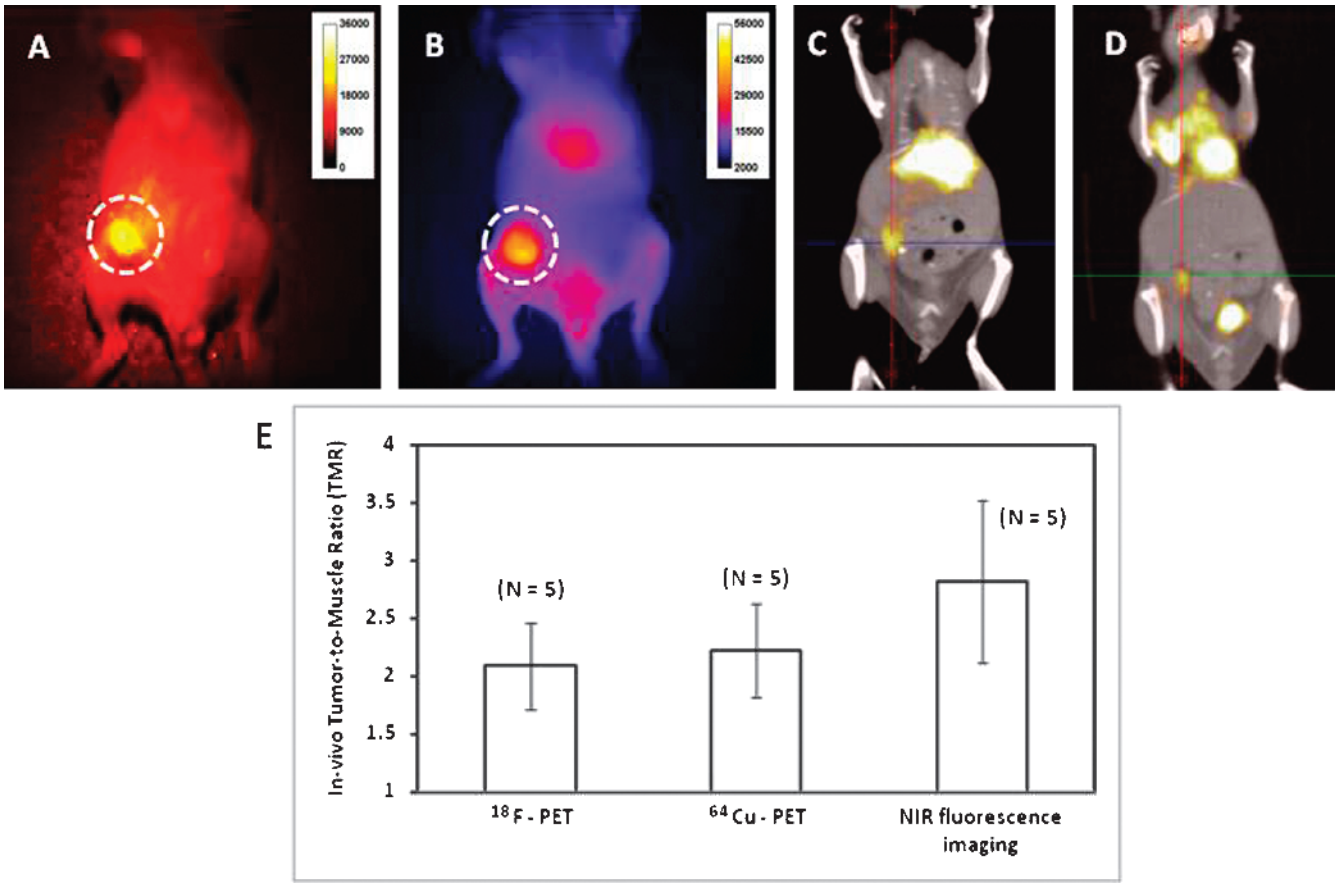

Figure 3. DsRed fluorescence imaging (A) shows the location of 4T1.2neu/R primary tumor in Balb/c mice, 2 weeks after subcutaneous inoculation into the mammary pad. NIR fluorescence (B) and PET/CT (C) imaging performed 24 hours after intravenous administration of $(^{64}Cu\text{-}DOTA)_n$-trastuzumab-$(IRDye800)_m$ shows uptake within the tumor. PET/CT images acquired 2 hours after administration of ^{18}FDG (D) also show tumor uptake. TMR determined from PET (^{18}F, ^{64}Cu) and NIR fluorescence imaging shows no statistical significance ($P > .1$) (E) and indicate that $(^{64}Cu\text{-}DOTA)_n$-trastuzumab-$(IRDye800)_m$ and ^{18}FDG are comparable with each other in detecting subcutaneous tumors.

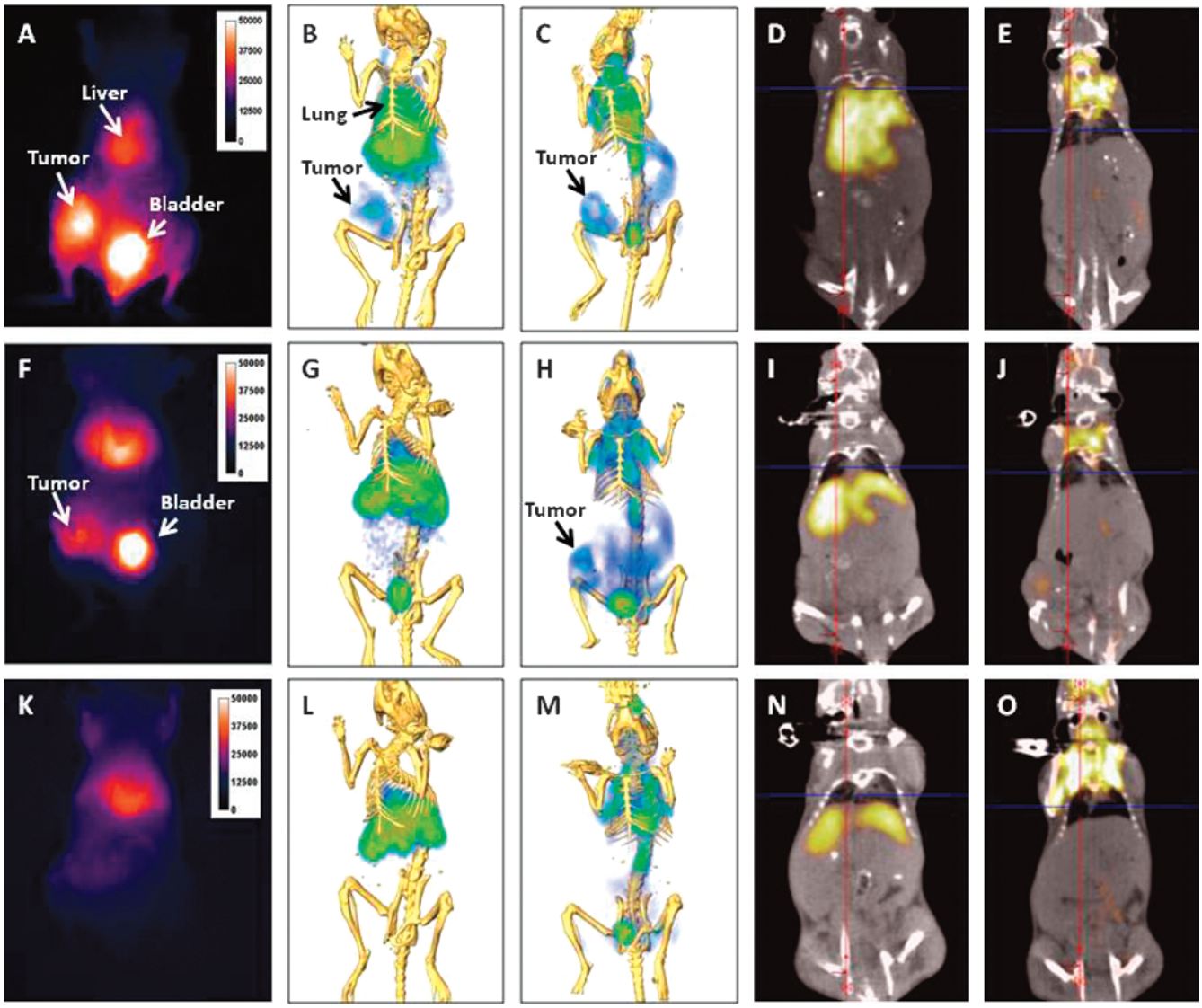

Figure 4. Comparison of $(^{64}\text{Cu-DOTA})_n$-trastuzumab-$(\text{IRDye800})_m$ and ^{18}FDG distribution on Balb/c mice subcutaneously inoculated with 4T1.2neu/R (A-E), 4T1.2/R (F-J), and non–tumor-bearing (K-O) mice. NIR fluorescence (A) and PET imaging with Cu-64 (B) and ^{18}FDG (C) showed uptake of imaging agents within the primary 4T1.2neu/R tumor. In mice inoculated with 4T1.2/R tumors, there was a reduction in accumulation of the dual-labeled agent within the primary tumor as shown with NIR fluorescence (F) and ^{64}Cu-PET (G) imaging, but ^{18}F-PET detected the 4T1.2/R tumor (H). Compared with 4T1.2/R (I, J) and non–tumor-bearing mice (M, O), PET/CT coronal section of 4T1.2neu/R tumor-bearing mice shows detection of lung metastases with the dual-labeled $(^{64}\text{Cu-DOTA})_n$-trastuzumab-$(\text{IRDye800})_m$ (D), whereas ^{18}FDG was not successful in detecting metastases (E).

PET imaging, but differences were observed in the *in vivo* distribution between the two imaging agents. *In vivo* TMRs between ^{18}FDG-PET, ^{64}Cu-PET, and NIR imaging ranged from 2.09 ± 0.37, 2.21 ± 0.40, and 2.81 ± 0.70, respectively (Figure 3*E*). No statistically significant differences ($P > .1$) between the TMR were observed between the modalities, indicating that the diagnostic capabilities of the molecularly specific dual-labeled imaging agent—$(^{64}\text{Cu-DOTA})_n$-trastuzumab-$(\text{IRDye800})_m$—are similar to those of clinically approved but nonspecific ^{18}FDG for detecting primary tumors.

Metastases in the 4T1.2 animal model are known to occur by 5 to 6 weeks [23]. To assess the imaging capabilities of $(^{64}\text{Cu-DOTA})_n$-trastuzumab-$(\text{IRDye800})_m$ in detecting HER-2–overexpressing metastatic lesions arising from the primary tumor, we acquired PET/CT and NIR fluorescence images after administration of the dual-labeled imaging agent in 4T1.2neu/R tumor-bearing Balb/c mice and compared the results with ^{18}FDG. We also compared uptake between non-tumor control, 4T1.2R, and 4T1.2neu/R tumor-bearing mice injected with $(^{64}\text{Cu-DOTA})_n$-trastuzumab-$(\text{IRDye800})_m$ and ^{18}FDG. Figure 4 shows NIR fluorescence, ^{64}Cu-PET, and ^{18}FDG-PET images from a representative mouse from each group. All mice showed nonspecific uptake of the dual-labeled imaging agent in the liver. The primary tumor region of the 4T1.2R tumor-bearing mice showed some uptake of the imaging agent, but there was significantly higher binding within the 4T1.2neu/R tumors as confirmed *ex vivo*. Nevertheless, because ^{18}FDG is molecularly nonspecific, it did not differentiate between the two tumor types, and we were able to detect both 4T1.2R and 4T1.2neu/R tumors. Although we were able to visualize the primary tumor with all modalities, ^{18}FDG-PET was not effective in detecting metastases. In contrast, we were able to detect multiple sites of 4T1.2neu/R metastases with the molecularly specific dual-labeled $(^{64}\text{Cu-DOTA})_n$-trastuzumab-$(\text{IRDye800})_m$. Owing to intrinsic differences between PET and NIR imaging capabilities, the metastatic lesions identified

through both modalities complemented each other. Lung metastases were clearly visualized noninvasively *in vivo* with ^{64}Cu-PET (Figure 4, *B* and *D*) in 4T1.2neu/R tumor-bearing mice, whereas limitations associated with scatter in deep tissue prevented detection with planar *in-vivo* NIR fluorescence imaging. Figure 4, *D* and *E*, *I* and *J*, and *N* and *O*, shows PET/CT sections acquired after (^{64}Cu-DOTA)$_n$-trastuzumab-(IRDye800)$_m$ and ^{18}FDG administration in representative 4T1.2neu/R, 4T1.2/R, and non–tumor-bearing mice, respectively. The crosshairs indicate lung location. ^{18}FDG-PET from both the tumor- and non–tumor-bearing mouse shows no accumulation within the lung. In contrast, ^{64}Cu-PET shows significant accumulation of the dual-labeled imaging agent within the lung region of a 4T1.2neu/R tumor-bearing mouse compared with the 4T1.2R and nontumor control.

The high spatial resolution achieved using NIR fluorescence imaging enabled us to detect metastatic lesions (~2 mm diameter) close to the skin (Figure 5, *A* and *B*), whereas PET imaging could not identify them. Optical imaging enabled us to visualize trafficking of the imaging agent from the primary tumor to proximal and distant lymph nodes when we removed the skin to reveal the mammary pad (Figure 5, *C* through *E*). This correlates with previous reports of lymphatic involvement in tumor growth and metastatic process of this animal model [26]. When we performed whole skin dissection of the tumor-bearing

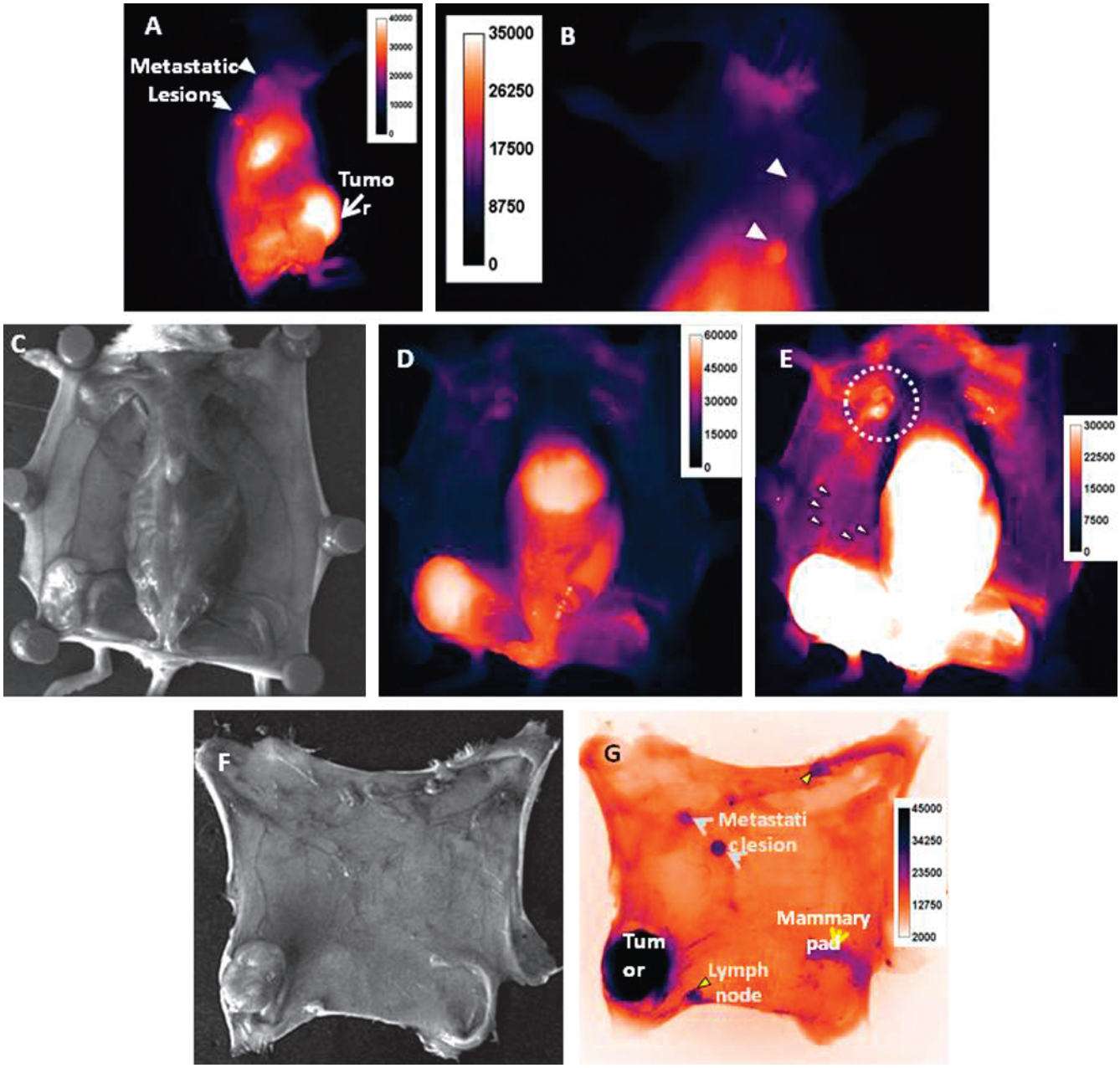

Figure 5. (^{64}Cu-DOTA)$_n$-trastuzumab-(IRDye800)$_m$ detected superficial skin metastases in Balb/c mice implanted with 4T1.2neu/R tumor as visualized by NIR fluorescence imaging (A, B). *Ex vivo* NIR fluorescence imaging revealed trafficking of the dual-labeled (^{64}Cu-DOTA)$_n$-trastuzumab-(IRDye800)$_m$ imaging agent from the primary tumor to distant lymph nodes (C-E). Whole-skin dissections showed accumulation of the imaging agent within the tumor, mammary pad, lymph nodes, and metastatic sites within the skin (F-G). All images in this figure have been acquired from the same mouse.

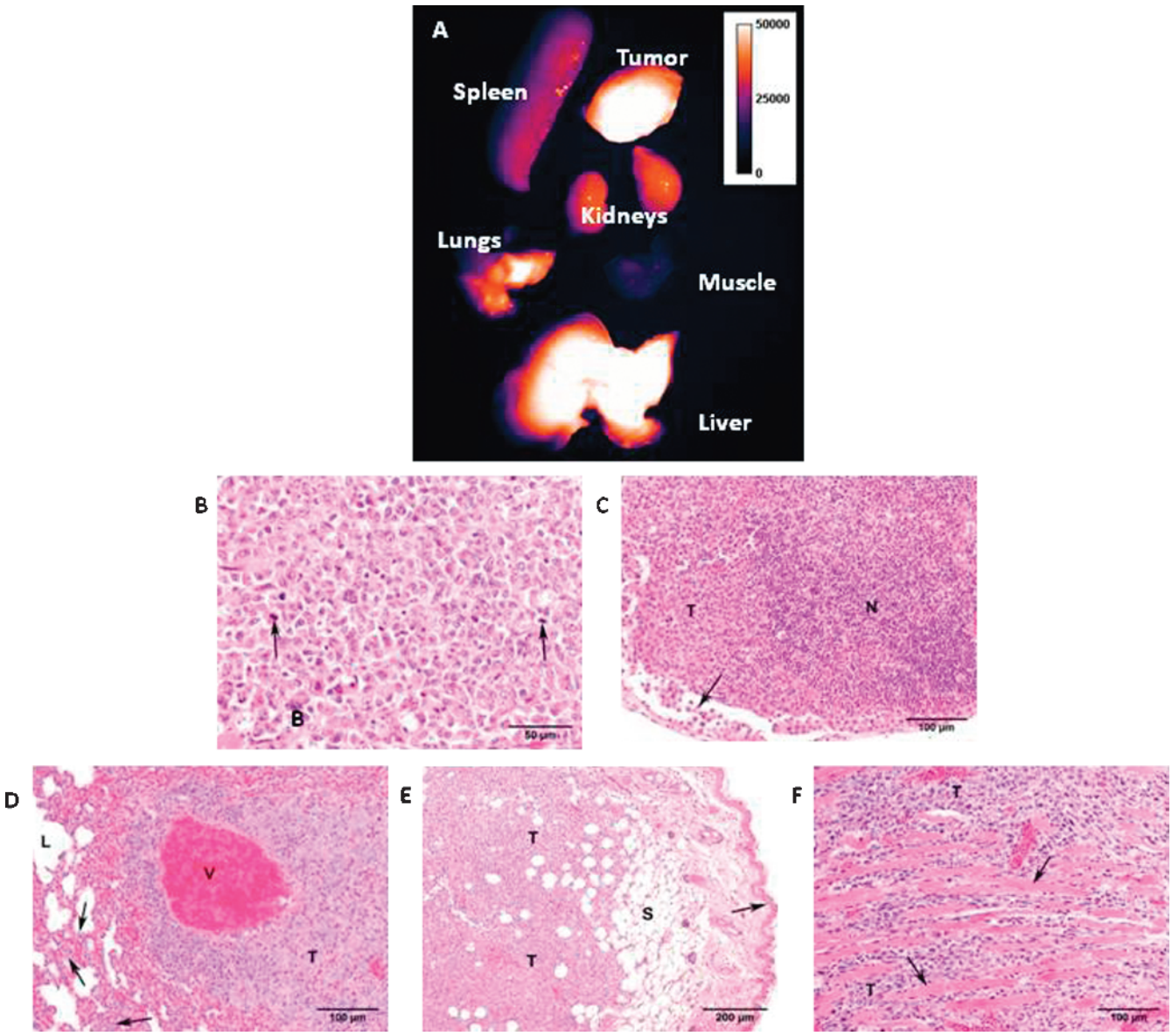

Figure 6. (A) *Ex vivo* NIR fluorescence imaging of organs harvested 24 hours after administration of $(^{64}Cu\text{-}DOTA)_n$-trastuzumab-$(IRDye800)_m$. Compared with muscle, there is high uptake in tumor, lung, and organs involved in antibody degradation, namely liver and kidneys. Spleen is enlarged because of the elevated levels of granulopoeisis and leukocytosis. Histologic H&E staining of representative primary 4T1.2neu tumor (B) and lymph node with a metastatic tumor (C) are shown. Arrows indicate numerous neoplastic cells in the subcapsular sinus. N indicates lymph node; T, tumor. Representative section of lung with a metastatic tumor (D) is shown with numerous neoplastic cells [T] seen around a pulmonary blood vessel. Also indicated are numerous circulating neutrophils in the alveolar septa (arrows) and in the large blood vessel [V]. L indicates alveolar space. We also observed skin (E) and skeletal muscle (F) metastases with arrows indicating numerous neoplastic cells (T) separating individual muscle fibers. S indicates skin.

mouse, in addition to visualizing the primary tumor, we observed accumulation of the imaging agent in lymph nodes and sections of the mammary pad. A representative photograph and NIR fluorescence image of a whole skin dissection is represented in Figure 5, *F* and *G*, respectively. In addition to the primary tumor, the tumor-draining lymph node (inguinal) is fluorescent and confirmed to be cancer-positive from H&E histologic staining. The skin metastatic lesions are also indicated.

We identified a total of 15 fluorescent lymph nodes from six tumor-bearing mice used in this study and performed further investigation using histologic staining. Only seven nodes were infiltrated by cancer cells. However, extensive inflammation and presence of granulopoieisis was observed in all the lymph nodes in addition to spleen and liver, consistent with previous reports [26–29]. Although *in vivo* whole-body NIR fluorescence imaging of $(^{64}Cu\text{-}DOTA)_n$-trastuzumab-$(IRDye800)_m$ did not show accumulation within the lung, we were able to confirm the presence of the imaging agent *ex vivo* on harvesting the organs after sacrifice (Figure 6*A*). Representative histologic H&E staining of the 4T1.2neu/R primary tumor and lung, lymph nodes, muscle, and skin metastases are shown in Figure 6, *B* to *F*.

We removed the skin of mice to reveal the mammary pad and compared whole skin dissections (Figure 7, *A*–*F*) within the three groups of mice to assess the specificity of $^{64}Cu\text{-}DOTA)_n$-trastuzumab-$(IRDye800)_m$ binding in lymph nodes. The nontumor control mice and the mice inoculated with 4T1.2/R did not show accumulation of the imaging agent within the mammary pad or lymph nodes. In

contrast, mice with 4T1.2neu/R tumors showed an increased background fluorescence signal within the entire skin in addition to sections of the mammary pad. Figure 7*F* shows another representative image where trafficking of the imaging agent from the primary tumor and its associated lymph node to the axillary region can be visualized.

We hypothesize that the NIR fluorescence signal from within lymph nodes and the mammary pad may be due to the interaction of the antibody-based imaging agent with elevated levels of HER-2/*neu* antigen expression as a result of the 4T1.2neu/R tumor.

The *ex vivo* NIR fluorescence LMR in 4T1.2neu/R tumor-bearing mice (2.85 ± 0.67) was found to be statistically higher in comparison with non–tumor-bearing mice (1.23 ± 0.15) with a $P < .05$ (Figure 7*H*). The large error bar found in the LMR in tumor-bearing mice can be due to the variability in the extent of lung metastases within each mouse.

Ex vivo NIR fluorescence TMR estimated from 4T1.2neu/R tumors (4.03 ± 0.57) was also found to be statistically higher than 4T1.2R tumors (1.83 ± 0.33) ($P < .05$) as shown in Figure 7*G*. LMR of 4T1.2neu/R tumor-bearing mice (2.85 ± 0.67) was found to be statistically higher in comparison with 4T1.2/R (1.45 ± 0.19) and non–tumor-bearing mice (1.23 ± 0.15) with a $P < .05$ (Figure 7*H*).

Discussion

According to the National Cancer Institute, approximately 191,000 new cases of breast cancer and 41,000 deaths were reported in 2009. Patient mortality and morbidity is often due to late-stage complications that arise from progression of the disease to distant metastatic sites. In breast cancer, the most common sites of metastases include lung, liver, bone, and brain. Metastasis is a complex and multistep process where the tumor cells have to detach from the primary tumor, enter the lymphatic or blood circulation, reach a distant site, attach, and proliferate. Molecular imaging techniques have immense potential in enhancing early stage diagnostics, monitoring treatment efficacy, and affecting drug discovery.

The 4T1 animal model was originally isolated by Fred Miller et al. [30] at the Karmanos Cancer Institute. By 6 weeks, 4T1 cells and subclones have been shown to metastasize to various organs including lungs,

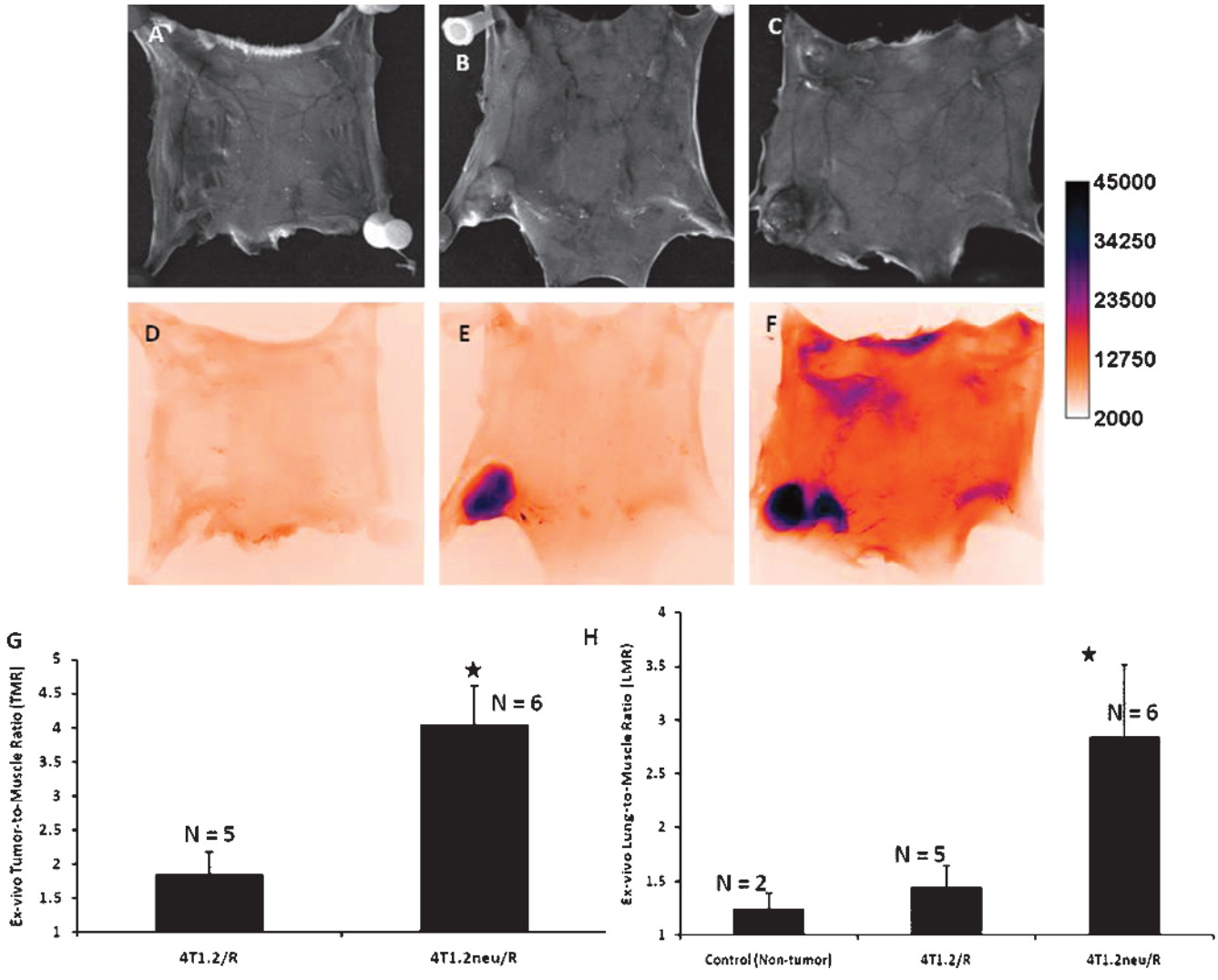

Figure 7. Comparison of *ex vivo* NIR fluorescence imaging of whole skin dissections between non–tumor-bearing (A, D), 4T1.2/R (B, E), and 4T1.2neu/R (C, F) tumor-bearing Balb/c mice 6 weeks after subcutaneous inoculation. TMR comparisons showed that there was significantly higher binding in 4T1.2neu/R tumors (4.03 ± 0.57) compared with 4T1.2/R tumors (1.83 ± 0.33; $P < .05$) (G). Also, quantitative LMR in 4T1.2neu/R tumor-bearing mice (2.85 ± 0.67) is significantly higher compared with 4T1.2/R (1.45 ± 0.19) and the non–tumor-bearing mice (1.23 ± 0.15), $P < .05$.

liver, and bone [23,26,31,32]. Although a number of investigators have used cancer cell lines expressing reporters to visualize cancer migration during metastases [33–39], very few studies have been performed where an exogenous diagnostic agent is administered to detect metastases within an animal model. In a recent report, Cao et al. [40] synthesized ^{64}Cu-DOTA-IL-18bp-Fc to assess the tumor-targeting efficiency and pharmacokinetics in interleukin-18 binding protein–sensitive cells using PET imaging in a lung metastases model. In the present study, we have demonstrated the targeting capabilities of $(^{64}\text{Cu-DOTA})_n$-trastuzumab-$(\text{IRDye800})_m$ *in vitro* using fluorescence microscopy and with an *in vivo* cancer model to assess uptake in primary tumors and subsequent metastases after intravenous administration of the imaging agent. Although there have been several studies using trastuzumab labeled for imaging with nuclear, magnetic resonance imaging, and optical techniques (see Table W1), this study is one of the first reports to use it in a dual-labeled diagnostic imaging agent to identify distant organ metastases. Because molecular-specific optical and nuclear probes have unique sets of advantages, combining modalities offers a wider range of opportunities for early detection of disease. Deep tissue penetration by radioactive isotopes enabled detection of lung metastases, whereas NIR fluorescence imaging provided information regarding lymphatic involvement. In addition to nonspecific radiocolloids used in the clinic, molecular imaging approaches such as these can potentially enhance the accuracy of nodal staging, although human trials will have to be conducted to confirm benefit.

Conclusions

Dual-labeled $(^{64}\text{Cu-DOTA})_n$-trastuzumab-$(\text{IRDye800})_m$ was tested for molecular specificity in HER-2–overexpressing breast cancer cells as well as in a relevant metastatic animal model to assess and confirm targeting *in vitro* and *in vivo*. Furthermore, we have compared the detection capabilities of the imaging agent with ^{18}FDG and have showed that $(^{64}\text{Cu-DOTA})_n$-trastuzumab-$(\text{IRDye800})_m$ has greater sensitivity in detection of metastases overexpressing HER-2.

References

[1] Cai W, Chen K, Li ZB, Gambhir SS, and Chen X (2007). Dual-function probe for PET and near-infrared fluorescence imaging of tumor vasculature. *J Nucl Med* **48**(11), 1862–1870.

[2] Chen K, Li ZB, Wang H, Cai W, and Chen X (2008). Dual-modality optical and positron emission tomography imaging of vascular endothelial growth factor receptor on tumor vasculature using quantum dots. *Eur J Nucl Med Mol Imaging* **35**(12), 2235–2244.

[3] Houston JP, Ke S, Wang W, Li C, and Sevick-Muraca EM (2005). Quality analysis of *in vivo* near-infrared fluorescence and conventional gamma images acquired using a dual-labeled tumor-targeting probe. *J Biomed Opt* **10**(5), 054010.

[4] Jarrett BR, Gustafsson B, Kukis DL, and Louie AY (2008). Synthesis of ^{64}Cu-labeled magnetic nanoparticles for multimodal imaging. *Bioconjug Chem* **19**(7), 1496–1504.

[5] Kim JS, An H, Rieter WJ, Esserman D, Taylor-Pashow KM, Sartor RB, Lin W, and Tarrant TK (2009). Multimodal optical and Gd-based nanoparticles for imaging in inflammatory arthritis. *Clin Exp Rheumatol* **27**(4), 580–586.

[6] Kimura RH, Miao Z, Cheng Z, Gambhir SS, and Cochran JR (2010). A dual-labeled knottin peptide for PET and near-infrared fluorescence imaging of integrin expression in living subjects. *Bioconjug Chem*, E-pub ahead of print.

[7] Li C, Wang W, Wu Q, Ke S, Houston J, Sevick-Muraca E, Dong L, Chow D, Charnsangavej C, and Gelovani JG (2006). Dual optical and nuclear imaging in human melanoma xenografts using a single targeted imaging probe. *Nucl Med Biol* **33**(3), 349–358.

[8] Ogawa M, Regino CA, Seidel J, Green MV, Xi W, Williams M, Kosaka N, Choyke PL, and Kobayashi H (2009). Dual-modality molecular imaging using antibodies labeled with activatable fluorescence and a radionuclide for specific and quantitative targeted cancer detection. *Bioconjug Chem* **20**(11), 2177–2184.

[9] Olson ES, Jiang T, Aguilera TA, Nguyen QT, Ellies LG, Scadeng M, and Tsien RY (2010). Activatable cell penetrating peptides linked to nanoparticles as dual probes for *in vivo* fluorescence and MR imaging of proteases. *Proc Natl Acad Sci USA* **107**(9), 4311–4316.

[10] Sampath L, Kwon S, Ke S, Wang W, Schiff R, Mawad ME, and Sevick-Muraca EM (2007). Dual-labeled trastuzumab-based imaging agent for the detection of human epidermal growth factor receptor 2 overexpression in breast cancer. *J Nucl Med* **48**(9), 1501–1510.

[11] Wang W, Ke S, Kwon S, Yallampalli S, Cameron AG, Adams KE, Mawad ME, and Sevick-Muraca EM (2007). A new optical and nuclear dual-labeled imaging agent targeting interleukin 11 receptor alpha-chain. *Bioconjug Chem* **18**(2), 397–402.

[12] Xu H, Baidoo K, Gunn AJ, Boswell CA, Milenic DE, Choyke PL, and Brechbiel MW (2007). Design, synthesis, and characterization of a dual modality positron emission tomography and fluorescence imaging agent for monoclonal antibody tumor-targeted imaging. *J Med Chem* **50**(19), 4759–4765.

[13] Yang L, Peng XH, Wang YA, Wang X, Cao Z, Ni C, Karna P, Zhang X, Wood WC, Gao X, et al. (2009). Receptor-targeted nanoparticles for *in vivo* imaging of breast cancer. *Clin Cancer Res* **15**(14), 4722–4732.

[14] Sampath L, Wang W, and Sevick-Muraca EM (2008). Near infrared fluorescent optical imaging for nodal staging. *J Biomed Opt* **13**(4), 041312.

[15] Slamon DJ, Godolphin W, Jones LA, Holt JA, Wong SG, Keith DE, Levin WJ, Stuart SG, Udove J, Ullrich A, et al. (1989). Studies of the HER-2/*neu* proto-oncogene in human breast and ovarian cancer. *Science* **244**(4905), 707–712.

[16] Gancberg D, Di Leo A, Cardoso F, Rouas G, Pedrocchi M, Paesmans M, Verhest A, Bernard-Marty C, Piccart MJ, and Larsimont D (2002). Comparison of HER-2 status between primary breast cancer and corresponding distant metastatic sites. *Ann Oncol* **13**(7), 1036–1043.

[17] Lopez-Guerrero JA, Llombart-Cussac A, Noguera R, Navarro S, Pellin A, Almenar S, Vazquez-Alvadalejo C, and Llombart-Bosch A (2006). HER2 amplification in recurrent breast cancer following breast-conserving therapy correlates with distant metastasis and poor survival. *Int J Cancer* **118**(7), 1743–1749.

[18] Simmons C, Miller N, Geddie W, Gianfelice D, Oldfield M, Dranitsaris G, and Clemons MJ (2009). Does confirmatory tumor biopsy alter the management of breast cancer patients with distant metastases? *Ann Oncol* **20**(9), 1499–1504.

[19] Tapia C, Savic S, Wagner U, Schonegg R, Novotny H, Grilli B, Herzog M, Barascud AD, Zlobec I, Cathomas G, et al. (2007). HER2 gene status in primary breast cancers and matched distant metastases. *Breast Cancer Res* **9**(3), R31.

[20] Carter P, Presta L, Gorman CM, Ridgway JB, Henner D, Wong WL, Rowland AM, Kotts C, Carver ME, and Shepard HM (1992). Humanization of an anti-p185HER2 antibody for human cancer therapy. *Proc Natl Acad Sci USA* **89**(10), 4285–4289.

[21] Cooper MS, Sabbah E, and Mather SJ (2006). Conjugation of chelating agents to proteins and radiolabeling with trivalent metallic isotopes. *Nat Protoc* **1**(1), 314–317.

[22] Cai W, Wu Y, Chen K, Cao Q, Tice DA, and Chen X (2006). *In vitro* and *in vivo* characterization of ^{64}Cu-labeled Abegrin, a humanized monoclonal antibody against integrin $\alpha_v\beta_3$. *Cancer Res* **66**(19), 9673–9681.

[23] Lelekakis M, Moseley JM, Martin TJ, Hards D, Williams E, Ho P, Lowen D, Javni J, Miller FR, Slavin J, et al. (1999). A novel orthotopic model of breast cancer metastasis to bone. *Clin Exp Metastasis* **17**(2), 163–170.

[24] Kim JH, Majumder N, Lin H, Chen J, Falo LD Jr, and You Z (2005). Enhanced immunity by NeuEDhsp70 DNA vaccine is needed to combat an aggressive spontaneous metastatic breast cancer. *Mol Ther* **11**(6), 941–949.

[25] Lindmo T, Boven E, Cuttitta F, Fedorka J, and Bunn PA (1984). Determination of the immunoreactive fraction of radiolabeled monoclonal antibodies by linear extrapolation to binding at infinite antigen excess. *J Immunol Methods* **72**, 77–89.

[26] Tao K, Fang M, Alroy J, and Sahagian GG (2008). Imagable 4T1 model for the study of late stage breast cancer. *BMC Cancer* **8**, 228.

[27] Bunt SK, Sinha P, Clements VK, Leips J, and Ostrand-Rosenberg S (2006). Inflammation induces myeloid-derived suppressor cells that facilitate tumor progression. *J Immunol* **176**(1), 284–290.

[28] DuPre SA and Hunter KW Jr (2007). Murine mammary carcinoma 4T1 induces a leukemoid reaction with splenomegaly: association with tumor-derived growth factors. *Exp Mol Pathol* **82**(1), 12–24.

[29] DuPre SA, Redelman D, and Hunter KW Jr (2007). The mouse mammary carcinoma 4T1: characterization of the cellular landscape of primary tumours and metastatic tumour foci. *Int J Exp Pathol* **88**(5), 351–360.

[30] Miller FR, Miller BE, and Heppner GH (1983). Characterization of metastatic heterogeneity among subpopulations of a single mouse mammary tumor: heterogeneity in phenotypic stability. *Invasion Metastasis* **3**(1), 22–31.

[31] Hiraga T, Williams PJ, Ueda A, Tamura D, and Yoneda T (2004). Zoledronic acid inhibits visceral metastases in the 4T1/luc mouse breast cancer model. *Clin Cancer Res* **10**(13), 4559–4567.

[32] Yoneda T, Michigami T, Yi B, Williams PJ, Niewolna M, and Hiraga T (2000). Actions of bisphosphonate on bone metastasis in animal models of breast carcinoma. *Cancer* **88**(12 suppl), 2979–2988.

[33] Amoh Y, Bouvet M, Li L, Tsuji K, Moossa AR, Katsuoka K, and Hoffman RM (2006). Visualization of nascent tumor angiogenesis in lung and liver metastasis by differential dual-color fluorescence imaging in nestin-linked-GFP mice. *Clin Exp Metastasis* **23**(7-8), 315–322.

[34] Hoshida T, Isaka N, Hagendoorn J, di Tomaso E, Chen YL, Pytowski B, Fukumura D, Padera TP, and Jain RK (2006). Imaging steps of lymphatic metastasis reveals that vascular endothelial growth factor-C increases metastasis by increasing delivery of cancer cells to lymph nodes: therapeutic implications. *Cancer Res* **66**(16), 8065–8075.

[35] Jenkins DE, Oei Y, Hornig YS, Yu SF, Dusich J, Purchio T, and Contag PR (2003). Bioluminescent imaging (BLI) to improve and refine traditional murine models of tumor growth and metastasis. *Clin Exp Metastasis* **20**(8), 733–744.

[36] Kaijzel EL, Snoeks TJ, Buijs JT, van der Pluijm G, and Lowik CW (2009). Multimodal imaging and treatment of bone metastasis. *Clin Exp Metastasis* **26**(4), 371–379.

[37] Kalikin LM, Schneider A, Thakur MA, Fridman Y, Griffin LB, Dunn RL, Rosol TJ, Shah RB, Rehemtulla A, McCauley LK, et al. (2003). *In vivo* visualization of metastatic prostate cancer and quantitation of disease progression in immunocompromised mice. *Cancer Biol Ther* **2**(6), 656–660.

[38] Kishimoto H, Kojima T, Watanabe Y, Kagawa S, Fujiwara T, Uno F, Teraishi F, Kyo S, Mizuguchi H, Hashimoto Y, et al. (2006). *In vivo* imaging of lymph node metastasis with telomerase-specific replication-selective adenovirus. *Nat Med* **12**(10), 1213–1219.

[39] Matsumoto S, Tanaka F, Sato K, Kimura S, Maekawa T, Hasegawa S, and Wada H (2009). Monitoring with a non-invasive bioluminescent *in vivo* imaging system of pleural metastasis of lung carcinoma. *Lung Cancer* **66**(1), 75–79.

[40] Cao Q, Cai W, Niu G, He L, and Chen X (2008). Multimodality imaging of IL-18–binding protein-Fc therapy of experimental lung metastasis. *Clin Cancer Res* **14**(19), 6137–6145.

[41] Smith-Jones PM, Solit DB, Akhurst T, Afroze F, Rosen N, and Larson SM (2004). Imaging the pharmacodynamics of HER2 degradation in response to Hsp90 inhibitors. *Nat Biotechnol* **22**(6), 701–706.

[42] Dijkers EC, Kosterink JG, Rademaker AP, Perk LR, van Dongen GA, Bart J, de Jong JR, de Vries EG, and Lub-de Hooge MN (2009). Development and characterization of clinical-grade ^{89}Zr-trastuzumab for HER2/*neu* immunoPET imaging. *J Nucl Med* **50**(6), 974–981.

[43] Dennis MS, Jin H, Dugger D, Yang R, McFarland L, Ogasawara A, Williams S, Cole MJ, Ross S, and Schwall R (2007). Imaging tumors with an albumin-binding Fab, a novel tumor-targeting agent. *Cancer Res* **67**(1), 254–261.

[44] Lub-de Hooge MN, Kosterink JG, Perik PJ, Nijnuis H, Tran L, Bart J, Suurmeijer AJ, de Jong S, Jager PL, and de Vries EG (2004). Preclinical characterisation of ^{111}In-DTPA-trastuzumab. *Br J Pharmacol* **143**(1), 99–106.

[45] Tang Y, Scollard D, Chen P, Wang J, Holloway C, and Reilly RM (2005). Imaging of HER2/*neu* expression in BT-474 human breast cancer xenografts in athymic mice using [(99m)Tc]-HYNIC-trastuzumab (Herceptin) Fab fragments. *Nucl Med Commun* **26**(5), 427–432.

[46] Tang Y, Wang J, Scollard DA, Mondal H, Holloway C, Kahn HJ, and Reilly RM (2005). Imaging of HER2/*neu*–positive BT-474 human breast cancer xenografts in athymic mice using (111)In-trastuzumab (Herceptin) Fab fragments. *Nucl Med Biol* **32**(1), 51–58.

[47] Artemov D, Mori N, Okollie B, and Bhujwalla ZM (2003). MR molecular imaging of the Her-2/*neu* receptor in breast cancer cells using targeted iron oxide nanoparticles. *Magn Reson Med* **49**(3), 403–408.

[48] Huh YM, Jun YW, Song HT, Kim S, Choi JS, Lee JH, Yoon S, Kim KS, Shin JS, Suh JS, et al. (2005). *In vivo* magnetic resonance detection of cancer by using multifunctional magnetic nanocrystals. *J Am Chem Soc* **127**(35), 12387–12391.

[49] Chen TJ, Cheng TH, Chen CY, Hsu SC, Cheng TL, Liu GC, and Wang YM (2009). Targeted Herceptin-dextran iron oxide nanoparticles for noninvasive imaging of HER2/*neu* receptors using MRI. *J Biol Inorg Chem* **14**(2), 253–260.

[50] Copland JA, Eghtedari M, Popov VL, Kotov N, Mamedova N, Motamedi M, and Oraevsky AA (2004). Bioconjugated gold nanoparticles as a molecular based contrast agent: implications for imaging of deep tumors using optoacoustic tomography. *Mol Imaging Biol* **6**(5), 341–349.

[51] Hilger I, Leistner Y, Berndt A, Fritsche C, Haas KM, Kosmehl H, and Kaiser WA (2004). Near-infrared fluorescence imaging of HER-2 protein over-expression in tumour cells. *Eur Radiol* **14**(6), 1124–1129.

[52] Koyama Y, Hama Y, Urano Y, Nguyen DM, Choyke PL, and Kobayashi H (2007). Spectral fluorescence molecular imaging of lung metastases targeting HER2/*neu*. *Clin Cancer Res* **13**(10), 2936–2945.

[53] Ogawa M, Regino CA, Choyke PL, and Kobayashi H (2009). *In vivo* target-specific activatable near-infrared optical labeling of humanized monoclonal antibodies. *Mol Cancer Ther* **8**(1), 232–239.

[54] Li-Shishido S, Watanabe TM, Tada H, Higuchi H, and Ohuchi N (2006). Reduction in nonfluorescence state of quantum dots on an immunofluorescence staining. *Biochem Biophys Res Commun* **351**(1), 7–13.

[55] Tada H, Higuchi H, Wanatabe TM, and Ohuchi N (2007). *In vivo* real-time tracking of single quantum dots conjugated with monoclonal anti-HER2 antibody in tumors of mice. *Cancer Res* **67**(3), 1138–1144.

Table W1. Review of Preclinical Imaging Using Trastuzumab to Target HER-2.

Imaging Modality	Imaging Agent	*In Vitro*/*In Vivo*: Cell Lines Used	Dose	Route	Reference
Nuclear medicine					
PET	^{64}Cu-DOTA-Herceptin	*In vivo* (mice): BT-474,	4 MBq	i.v.	[41]
	^{68}Ga-DOTA-F(ab′)2	MCF-7, MDA-MB-468 (s.c.)	309 MBq		
	^{89}Zr-trastuzumab	*In vivo* (mice): SKOV3,	100 μg of trastuzumab,		
		GLC4 (s.c.)	1 MBq	i.v.	[42]
SPECT/CT	^{111}In-DOTA-Fab4D5,	*In vivo* (mice): tumors	4 mg/kg (300-500 μCi)	i.v.	[43]
	^{111}In-DOTA-AB.Fab4D5	cells derived from MMTV/HER-2 transgenic mice (s.c.)	25 MBq (30 μg)	i.v.	[44–46]
Scintigraphy (whole body)	[^{99m}Tc]-HYNIC-trastuzumab Fab,	*In vivo* (mice): BT474,	3.7 MBq (30 μg)		
	^{111}In-trastuzumab Fab,	SK-OV-3 (s.c.)			
	^{111}In-DTPA-trastuzumab	*In vivo* (mice, humans)	Mice: 450 ± 25 kBq (25 μg); human: 100-150 MBq (5 mg)	i.v.	
Scintillation counter (tissue/cells)	^{111}In-DOTA-Herceptin,	*In vivo* (mice): BT474 (s.c.)	1.6 MBq	i.v.	[41]
	^{111}In-DOTA-F(ab′)2,	*In vitro*: MCF-7, SKBr-3			
	^{111}In-CHX-A -DTPA-Herceptin,				
	^{90}Y-DTPA-Herceptin				
Magnetic resonance tomography	WSIO-Herceptin	*In vivo* (mice): NIH3T6.7 (s.c.)	400 μg of Fe	i.v.	[47,48]
	Biotinylated Herceptin with streptavidin-SPIO microbeads	*In vitro*: MCF-7, MDA-MB-231, AU-565 (gel phantoms)	2-50 × 10^{10} biotin/μl		
	Herceptin nanoparticles	*In vivo* (mice): SKBr3, KB	20 μmol/kg	i.v.	[49]
Optoacoustic tomography	Herceptin conjugated with gold nanoparticles (MabNP)	*In vitro*: SKBR3, BT-474, MDA-MB-231, and MCF-7	10^9 Mab/NP		[50]
Optical imaging					
Fluorescence imaging	Cy5.5-labeled Herceptin	*In vitro*: SK-BR-3, L6 rat myoblasts	100 μg	i.v.	[51]
	Herceptin-RhodG	*In vivo* (mice): SK-BR-3, PE/CA-PJ34 (s.c.)	50 μg in 200 μl of PBS	i.v.	[52]
	Tra-Cy5.5 (SQ)	*In vivo* (mice): 3T3/HER-2+,	50 μg/100 μl of PBS	i.v.	[53]
	Tra-Alexa680(SQ)	Balb/3T3/HER-2− (s.c.)			
Fluorescence quantum dots	Trastuzumab-Qdots	*In vivo* (mice): 3T3/HER-2+, Balb/3T3/HER-2−	2 μM (100 μl), 5-6 μm tissue sections stained with 10 nM	i.v.	[54,55]
		In vivo (mice), *Ex vivo* (tumor from mice): KPL-4, MBA-MB-231 (s.c.)			
Dual-labeled imaging agents (nuclear and optical)	(^{111}In-DTPA)$_n$-trastuzumab-(IRDye800)$_m$	*In vitro*: SKBr3 and MDA-MB-231			[10,14]
		In vivo: SKBr3-luc (s.c.)	80-200 μg (70-200 μCi)	i.v., i.d.	

i.v. indicates intravenous; s.c., subcutaneous; i.d., intradermal.